

Gas Inflow and Metallicity Drops in Star-forming Galaxies

Daniel Ceverino^{1,2*}, Jorge Sánchez Almeida^{3,4}, Casiana Muñoz Tuñón^{3,4},
Avishai Dekel⁵, Bruce G. Elmegreen⁶, Debra M. Elmegreen⁷, Joel Primack⁸

¹Centro de Astrobiología (CSIC-INTA), Ctra de Torrejón a Ajalvir, km 4, E-28850 Torrejón de Ardoz, Madrid, Spain

²Astro-UAM, Universidad Autónoma de Madrid, Unidad Asociada CSIC, E-28049 Madrid, Spain

³Instituto de Astrofísica de Canarias, E-38205 La Laguna, Tenerife, Spain

⁴Departamento de Astrofísica, Universidad de La Laguna, E-38205 La Laguna, Tenerife, Spain

⁵Center for Astrophysics and Planetary Science, Racah Institute of Physics, The Hebrew University, Jerusalem 91904, Israel

⁶IBM Research Division, T.J. Watson Research Center, 1101 Kitchawan Road, Yorktown Heights, NY 10598, USA

⁷Department of Physics and Astronomy, Vassar College, Poughkeepsie, NY 12604, USA

⁸Department of Physics, University of California, Santa Cruz, CA, 95064, USA

ABSTRACT

Gas inflow feeds galaxies with low metallicity gas from the cosmic web, sustaining star formation across the Hubble time. We make a connection between these inflows and metallicity inhomogeneities in star-forming galaxies, by using synthetic narrow-band images of the $H\alpha$ emission line from zoom-in AMR cosmological simulations of galaxies with stellar masses of $M_* \simeq 10^9 M_\odot$ at redshifts $z = 2 - 7$. In $\sim 50\%$ of the cases at redshifts lower than 4, the gas inflow gives rise to star-forming, $H\alpha$ -bright, off-centre clumps. Most of these clumps have gas metallicities, weighted by $H\alpha$ luminosity, lower than the metallicity in the surrounding interstellar medium by ~ 0.3 dex, consistent with observations of chemical inhomogeneities at high and low redshifts. Due to metal mixing by shear and turbulence, these metallicity drops are dissolved in a few disc dynamical times. Therefore, they can be considered as evidence for rapid gas accretion coming from cosmological inflow of pristine gas.

Key words: cosmology — galaxies: evolution — galaxies: formation

1 INTRODUCTION

A number of observational works have detected chemical inhomogeneities in the gas of star-forming galaxies, both at high redshift (Cresci et al. 2010; Queyrel et al. 2012) and in the local universe (Richards et al. 2014; see Sánchez Almeida et al. 2014a for a review). Most galaxies develop negative metallicity gradients, with the metallicity decreasing inside-out (Edmunds & Greenhow 1995; van Zee et al. 1998; Magrini et al. 2007; Sánchez et al. 2014; Stott et al. 2014; Kehrig et al. 2015). On top of such large-scale variation, many galaxies show localized, kpc-size starbursts with the metallicity in the burst lower than in the surrounding interstellar medium (Sánchez Almeida et al. 2013, 2014b, 2015). These metallicity drops are of the order of 0.3 dex or larger. Since the time-scale for gas mixing in disk galaxies is expected to be short, on the order of the rotational period or shorter (de Avillez & Mac Low 2002; Yang & Krumholz

2012; Petit et al. 2015), the low-metallicity gas sustaining the starbursts must have arrived to the galaxies recently.

A plausible interpretation of these observations is the triggering of star-formation by gas recently accreted from the cosmic web (Cresci et al. 2010; Sánchez Almeida et al. 2013, 2015). Numerical simulations predict that the inflow of cosmic-web gas has sustained star formation in galaxies along the Hubble time (Dekel et al. 2013, and references therein). The gas being accreted is metal-poor (van de Voort & Schaye 2012) and it is expected to induce giant star-forming clumps in early disks (Dekel et al. 2009; Ceverino et al. 2010; Mandelker et al. 2014). The gas from the web may trigger a starburst as it gets compressed when approaching the disk, or it builds up the gas mass in the disk which eventually gives rise to starbursts due to internal instabilities. Only if the buildup and triggering occurs rather fast, in a time-scale similar to or shorter than the mixing time-scale, the recently accreted, low-metallicity gas can still dominate the mass of the star-forming clumps.

This paper studies whether this conjecture is valid in cosmological simulations of galaxies, namely whether metal-poor star-forming gas clumps in high- z protogalaxies

* E-mail: daniel.ceverino@cab.inta-csic.es

can be associated with individual gas accretion events. Verbeke et al. (2014) simulate the effect of gas clouds falling into disks of various masses and types. Their conclusion is that gas accretion may give rise to low metallicity starbursts depending on details of the accretion event, such as the accreted gas mass, the impact parameter of the stream, or whether the orbit is prograde or retrograde. These simulations are idealized with ad-hoc initial conditions. We want to see whether the phenomena of metallicity drops associated with cosmic gas accretion appear in a cosmological setup, where gas infall is not imposed but appears naturally, as a result of the formation of large-scale structures.

We aim at studying and characterizing the physical process, rather than at explaining a particular set of observations. However, we want to make predictions that connect a given observable such as the gas metallicity weighted by $H\alpha$ luminosity, with cosmological gas inflow. In section §2 we describe the sample of simulations. §3 describes the mock $H\alpha$ images of the sample. §4 discusses the metallicity drops found in the simulations and we connect them with recent gas accretion events in §5. Finally, §6 is devoted to discussion and summary.

2 SIMULATIONS

The zoom-in simulations used in this paper were drawn from a larger dataset, the VELA sample (Ceverino et al. 2014; Zolotov et al. 2015). We select for each simulation the latest snapshot that fulfills the two following criteria:

- A galaxy stellar mass of $M_* \leq 10^9 M_\odot$,
- A specific star-formation-rate of $sSFR \geq 1 \text{ Gyr}^{-1}$,

where $sSFR = SFR/M_*$ (Table 1). Therefore, we select star-forming galaxies with low masses ($M_* = (0.4 - 1) 10^9 M_\odot$), and gas rich (gas-over-star mass ratio about unity) at high-redshifts ($z = 6.7 - 1.9$). These protogalaxies are expected to undergo large, quasi-continuous gas inflows, so that they are the best candidates for setting the connection between cosmological gas inflow and metallicity drops. Ongoing or recent major mergers with strong inflows of stars and dark matter could complicate this connection, so that they are excluded from the analysis.

The simulations were performed with the ART code (Kravtsov et al. 1997; Kravtsov 2003), which accurately follows the evolution of a gravitating N-body system and the Eulerian gas dynamics using an AMR approach. Beyond gravity and hydrodynamics, the code incorporates many of the physical processes relevant for galaxy formation. These processes, representing subgrid physics, include gas cooling by atomic hydrogen and helium, metal and molecular hydrogen cooling, photoionization heating by a constant cosmological UV background with partial self-shielding, star formation and feedback, as described in Ceverino & Klypin (2009), Ceverino et al. (2010), and Ceverino et al. (2014). In addition to thermal-energy feedback, the simulations use radiative feedback. This model adds a non-thermal pressure, radiation pressure, to the total gas pressure in regions where ionizing photons from massive stars are produced and trapped. In the current implementation, named RadPre in Ceverino et al. (2014),

Table 1. Properties of the zoom-in simulations, ordered by decreasing gas fraction. Columns show name of the run, redshift, virial radius, virial mass, stellar mass, gas mass within $0.1R_{\text{vir}}$ and SFR in $M_\odot \text{ yr}^{-1}$. Masses are in M_\odot and radii in kpc. Virial properties are computed using an overdensity, $\Delta(z) \simeq 180$, above mean density (Dekel et al. 2013; Bryan & Norman 1998).

| Run | z | R_{vir} | virial mass | stellar mass | gas mass | SFR |
|-----|-----|------------------|----------------------|-------------------|-------------------|-----|
| V05 | 3.0 | 31 | 5.3×10^{10} | 4.0×10^8 | 5.9×10^8 | 0.5 |
| V09 | 5.2 | 20 | 5.2×10^{10} | 5.2×10^8 | 6.0×10^8 | 2.2 |
| V22 | 6.1 | 17 | 5.1×10^{10} | 6.2×10^8 | 6.8×10^8 | 4.3 |
| V07 | 4.9 | 18 | 3.3×10^{10} | 5.2×10^8 | 5.7×10^8 | 3.0 |
| V01 | 3.5 | 26 | 4.5×10^{10} | 4.5×10^8 | 4.6×10^8 | 1.2 |
| V04 | 1.9 | 55 | 12×10^{10} | 10×10^8 | 10×10^8 | 2.6 |
| V06 | 5.2 | 20 | 5.5×10^{10} | 5.9×10^8 | 5.8×10^8 | 3.2 |
| V26 | 4.9 | 22 | 5.9×10^{10} | 5.7×10^8 | 5.3×10^8 | 4.0 |
| V17 | 6.7 | 16 | 5.1×10^{10} | 5.6×10^8 | 5.0×10^8 | 5.0 |
| V13 | 3.3 | 33 | 8.1×10^{10} | 7.8×10^8 | 6.9×10^8 | 2.3 |
| V02 | 2.7 | 37 | 7.0×10^{10} | 8.1×10^8 | 5.9×10^8 | 1.1 |
| V25 | 3.5 | 32 | 8.8×10^{10} | 8.3×10^8 | 5.7×10^8 | 2.2 |
| V23 | 4.0 | 27 | 6.6×10^{10} | 10×10^8 | 6.2×10^8 | 2.8 |
| V27 | 3.8 | 32 | 9.9×10^{10} | 8.9×10^8 | 5.1×10^8 | 0.9 |
| V08 | 3.2 | 33 | 7.1×10^{10} | 9.9×10^8 | 4.8×10^8 | 1.4 |
| V33 | 4.5 | 25 | 7.6×10^{10} | 9.5×10^8 | 4.5×10^8 | 2.4 |
| V20 | 6.1 | 16 | 3.9×10^{10} | 8.3×10^8 | 3.5×10^8 | 2.3 |

radiation pressure is included in the cells (and their closest neighbors) that contain stellar particles younger than 5 Myr and whose gas column density exceeds 10^{21} cm^{-2} .

Metals are produced and advected according to the model described in Kravtsov (2003). The code follows two kinds of metals: metals produced in SN-II (Oxygen and other α -elements), and metals produced in SN-Ia (Iron-like elements). Stars with masses between $m_* = 8 M_\odot$ and $100 M_\odot$ eject $f_Z m_*$ mass of metals in core-collapsed supernovae, where $f_Z = \min(0.2, 0.01 m_* - 0.06)$, which crudely approximates the SN yields of Woosley & Weaver (1995). After integrating a Chabrier IMF, this translates into the ejection of $\sim 1\%$ of the initial stellar mass of a particle representing a single stellar population. These metals are injected in the cell hosting the star particle at a constant rate during 40 Myr, the time that takes the last SN-II to explode.

The initial conditions of these runs contain from 6.4 to $46 \cdot 10^6$ dark matter particles with a minimum mass of $8.3 \times 10^4 M_\odot$, while the particles representing single stellar populations that were formed in the simulation have a minimum mass of $10^3 M_\odot$. The maximum spatial resolution is between 17-35 proper pc. More details can be found in Ceverino et al. (2014) and Zolotov et al. (2015).

3 $H\alpha$ IMAGES

If we want to make a connection between the gas inflow and the metallicity drops in starburst regions, the first step is to generate synthetic narrowband observations of $H\alpha$ emission that highlights star-forming regions. The mock $H\alpha$ images of the sample are generated according to the method outlined in Ceverino et al. (2012). In short, we first compute the star formation rate density, ρ_{SFR} , using the distribution of stellar particles younger than 50 Myr. Then, we compute the $H\alpha$

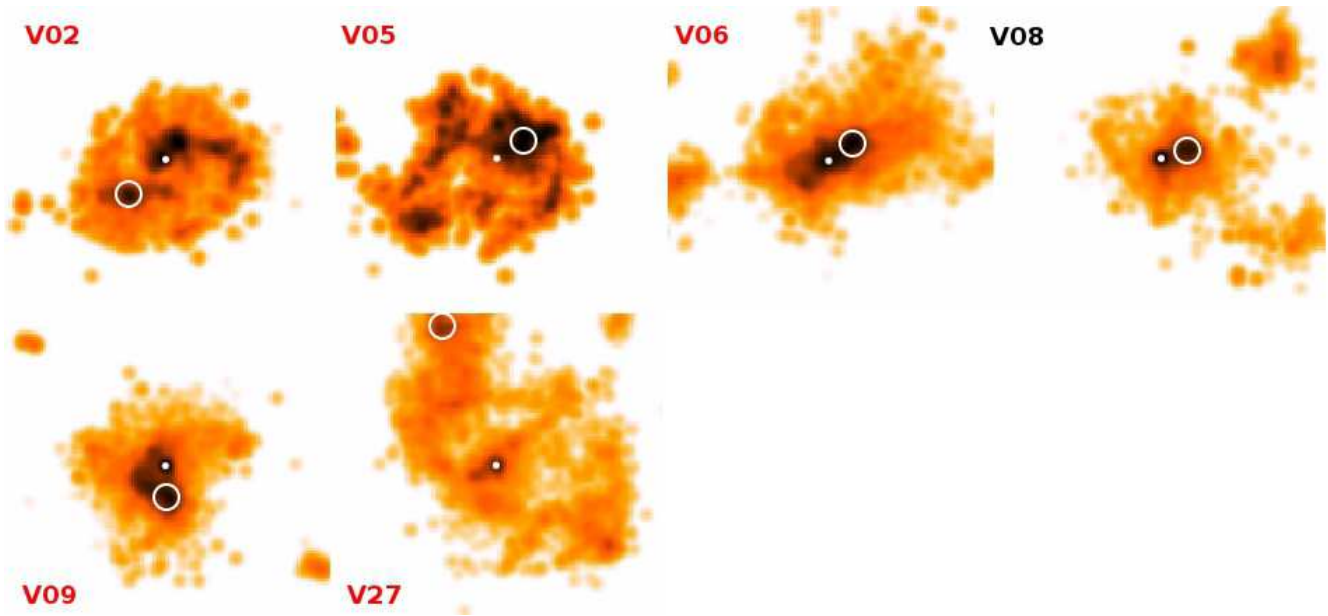


Figure 1. Synthetic $H\alpha$ maps of galaxies with off-centre bright clumps, marked by a white circle with a radius of 0.4 kpc. A white dot marks the galaxy center of mass. The size of each image is $10 \times 10 \text{ kpc}^2$. In most of these runs, the clumps have a metallicity lower than in the inter-clump medium (red labels). A single case with a slightly off-center clump with metallicity higher than in the inter-clump is labeled in black.

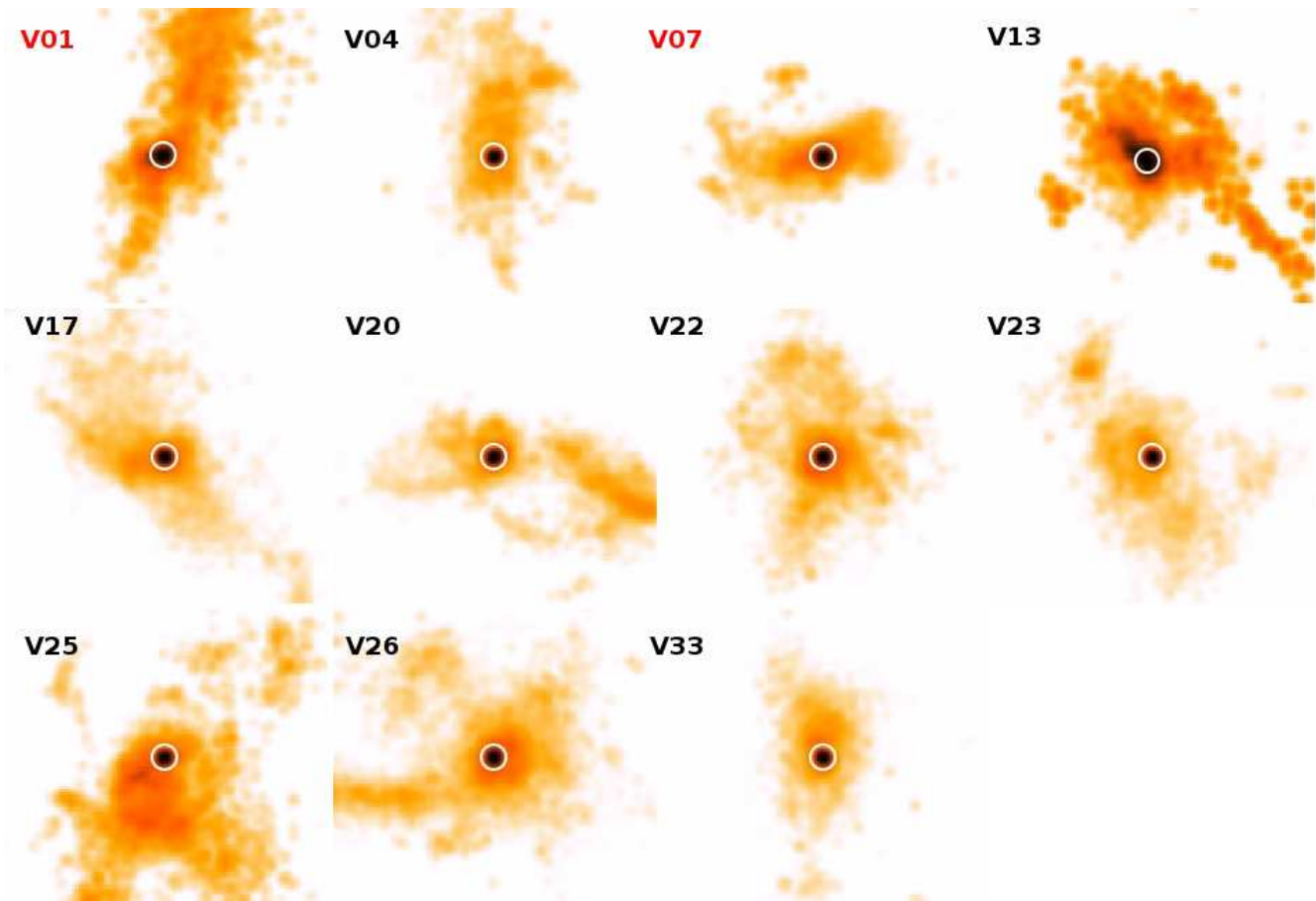


Figure 2. Synthetic $H\alpha$ maps of galaxies with only one bright central clump marked by the white circle. The size of the images and the labels are as in Figure 1. 2 out of 11 cases show metallicity drops at the galaxy centre.

emissivity $\epsilon_{\text{H}\alpha}$, based on the Kennicutt (1998) conversion, adjusted to a Chabrier (2003) IMF,

$$\log \epsilon_{\text{H}\alpha} = \log \rho_{\text{SFR}} + 41.33, \quad (1)$$

where $\epsilon_{\text{H}\alpha}$ is in $\text{erg s}^{-1} \text{kpc}^{-3}$ and ρ_{SFR} is in $M_{\odot} \text{yr}^{-1} \text{kpc}^{-3}$. This equation holds as long as the $\text{H}\alpha$ photons trace the underlying star-formation events, which is the case on scales of a few hundred parsecs (Kennicutt et al. 2007). The $\text{H}\alpha$ surface brightness is obtained by integrating the emissivity along a line-of-sight parallel to the galaxy rotation axis (face-on view). Radiative transfer effects and dust extinction are not considered. However, these effects are small in these dwarf galaxies, where the dust column density is low (Fisher et al. 2014, Sánchez Almeida et al., submitted). A Gaussian smoothing of FWHM=0.3 kpc is implemented in the final images.

The galaxies are classified in two groups, according to their morphology in the face-on, $\text{H}\alpha$ images. The first group looks clumpy in $\text{H}\alpha$, showing one or more $\text{H}\alpha$ -bright, off-centre clumps (Figure 1). The second group shows only one $\text{H}\alpha$ -bright clump at the galaxy centre (Figure 2). These $\text{H}\alpha$ -bright clumps could be associated with the starburst regions observed in star-forming galaxies at high and low redshifts (Genzel et al. 2011; Sánchez Almeida et al. 2014b).

Around one-third of the sample of star-forming galaxies are clumpy. This clumpy fraction increases to $\sim 50\%$ if we exclude redshifts higher than 4. This is consistent with UV observations of bright clumps in high- z galaxies (Guo et al. 2015). Their figure 10 shows a 60% fraction of clumpy galaxies with stellar masses of $\log(M_*/M_{\odot})=9-10$ in the redshift range $z = 0.5-3$, slightly higher masses than in our sample, (see also Elmegreen et al. (2007) and Tadaki et al. (2014)).

4 METALLICITY DROPS

The next step is to find the metallicity drops by computing the mean gas metallicity, weighted by $\text{H}\alpha$ emissivity, of the $\text{H}\alpha$ -bright clumps and the inter-clump medium. We translate the gas density of metals produced by supernova type-II into oxygen abundances by using the formula described in Mandelker et al. (2014),

$$\frac{O}{H} = \frac{f_O z_{\text{SNII}}}{X A} = \frac{0.5 z_{\text{SNII}}}{0.755 \times 16} \quad (2)$$

where z_{SNII} is the metal-to-gas mass ratio within a cell, $X = 0.755$ is the hydrogen mass fraction, and $A = 16$ is the atomic weight of oxygen. We also assume that half of the mass in metals released in SNII are oxygen atoms ($f_O = 0.5$), roughly based on Woosley & Weaver (1995). The actual values of the scaling factors do not affect our results which are based on metallicity ratios rather than on the absolute value of the metallicities.

The $\text{H}\alpha$ -weighted gas metallicities are measured in circular apertures of radius 0.4 kpc, centered on the brightest off-center clump in $\text{H}\alpha$ for each clumpy galaxy (Figure 1). For the non-clumpy galaxies (Figure 2), the aperture is centered at the $\text{H}\alpha$ -bright clump at the galaxy center of mass. In this first approach, we ignore all the smaller (dimmer) clumps, because they are usually not observed

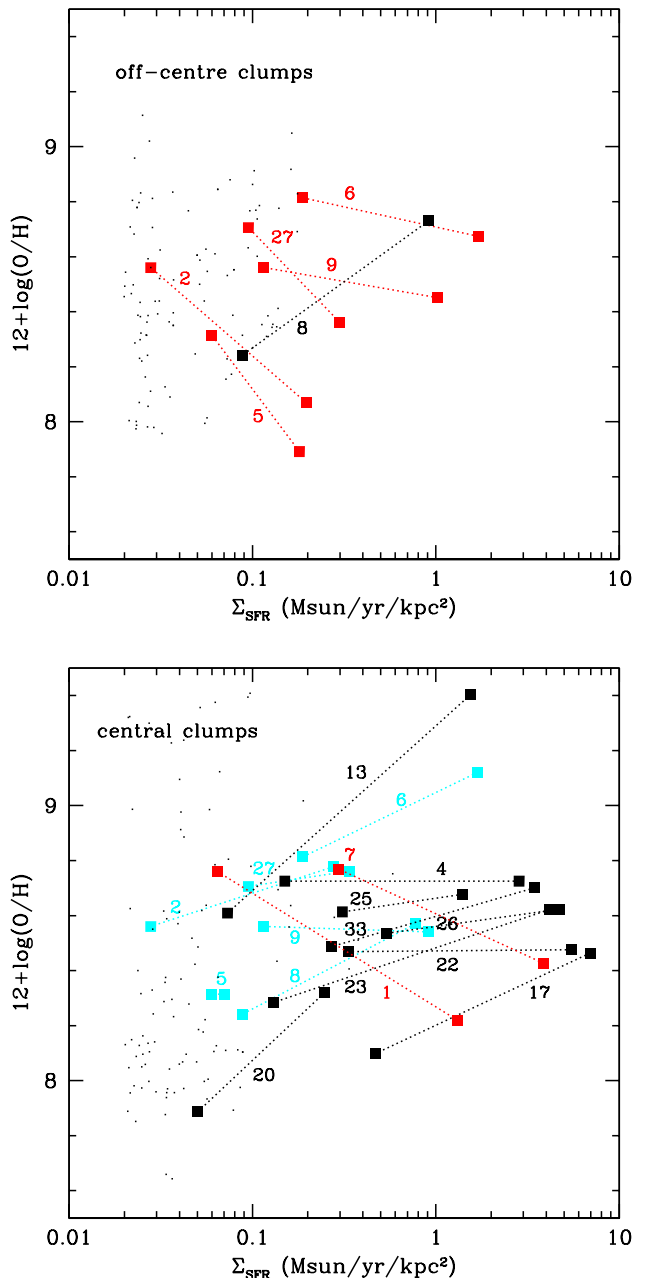


Figure 3. Metallicity versus SFR surface density measured in apertures of 0.4 kpc radius. Each galaxy has two measures, linked by a dotted line, labeled by the run ID. The highest SFR value in each galaxy corresponds to the $\text{H}\alpha$ -bright clump. The lowest value corresponds to a randomly placed aperture. The small dots represent 100 random apertures for V02 (top) and V13 (bottom), excluding the $\text{H}\alpha$ -bright clump and the galaxy centre. The squares are joined by red or black lines depending on whether the clump is metal poorer or metal richer than the inter-clump medium. Cyan squares and lines correspond to the center of clumpy galaxies.

in the galaxies of this mass scale. Therefore, we focus on the brightest clump that usually corresponds to the head in observed tadpole galaxies (Elmegreen & Elmegreen 2010; Elmegreen et al. 2012). This is where a large amount of gas is needed to feed high SFRs.

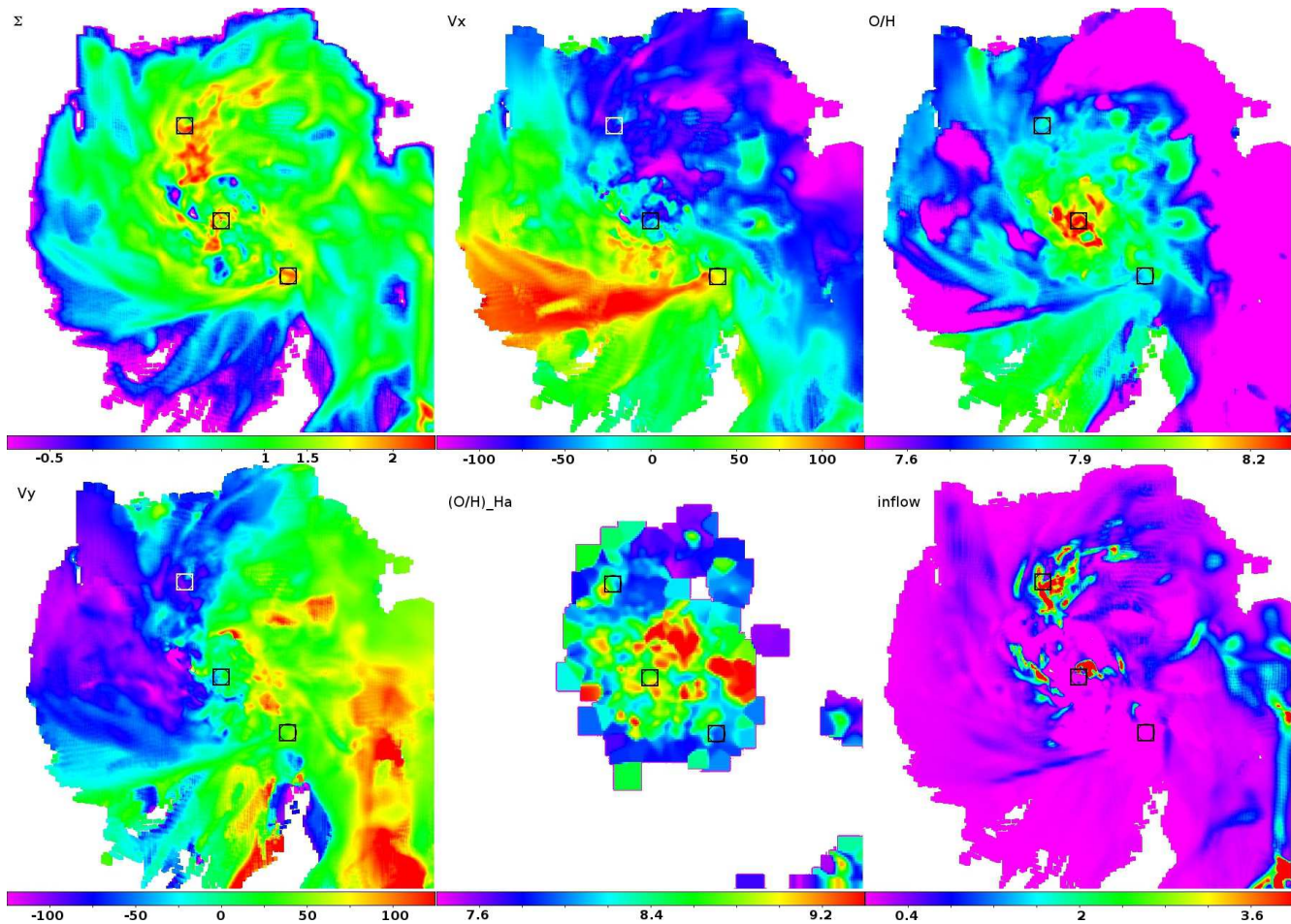


Figure 4. Face-on maps of gas surface density (Σ), velocity in the X-axis of the galaxy plane (V_X), metallicity (O/H), velocity in the Y-axis (V_Y), gas metallicity weighted by $H\alpha$ emissivity ($O/H_{H\alpha}$), and radial inflow of V27 at $z = 3.8$. In each panel, three square apertures mark the galaxy center and two regions with low metallicity at the end of two incoming streams of pristine gas. Both apertures are close to $H\alpha$ -bright star-forming regions. The size of the images is $20 \times 20 \text{ kpc}^2$.

In addition to the aperture centered on the clump, we also consider another aperture randomly placed in the inter-clump medium with a SFR surface density close to the galaxy median value. Therefore, each galaxy has two metallicity measures. The apertures centered on $H\alpha$ -bright clumps have a high SFR surface density, much higher than in the inter-clump medium. The actual position of the aperture chosen for reference does not change the conclusions significantly, as shown by 100 different random apertures for V02 and V13.

The top panel of Figure 3 shows the metallicity in the clumpy galaxies of Figure 1. The galaxies with metallicity drops are shown using red symbols and lines in Figure 3. In almost all cases, the gas metallicity in the clump is significantly lower than the metallicity of the inter-clump medium. The median drop in metallicity is 0.33 dex with a maximum value of 0.5 dex (V02). The only case of an off-centered clump without a metallicity drop is shown in V08. This clump is also the nearest to the center of mass, so this could be an intermediate case between off-centered and central clumps.

The central clumps of Figure 2 have higher SFR densities than the off-centered clumps, most probably

because these galaxies are more compact than their clumpy counterparts. The metallicity of the central clump is similar to or higher than the metallicity of the galaxy. More than 50% of the random apertures described above have metallicities lower than the central value. This is consistent with the fact that irregular galaxies with steep inner profiles could have negative metallicity gradients (Pilyugin et al. 2015). V1 and V7 are two exceptional cases that show a central metallicity which is ~ 0.5 dex lower than the metallicity at larger radii. In these cases, large radial flows of gas decrease the metallicity at the center.

It is remarkable that the $H\alpha$ -bright, off-centre clumps have lower metallicities than other star-forming regions with lower $H\alpha$ luminosities, because these clumps have high star formation rates and they are regions where significant amount of metals are injected into the gas due to supernova explosions. These regions must have accreted large amounts of gas with low-metallicity, possibly coming from streams of inflowing gas. This inflow of low-metallicity gas could explain these inhomogeneities in metallicity.

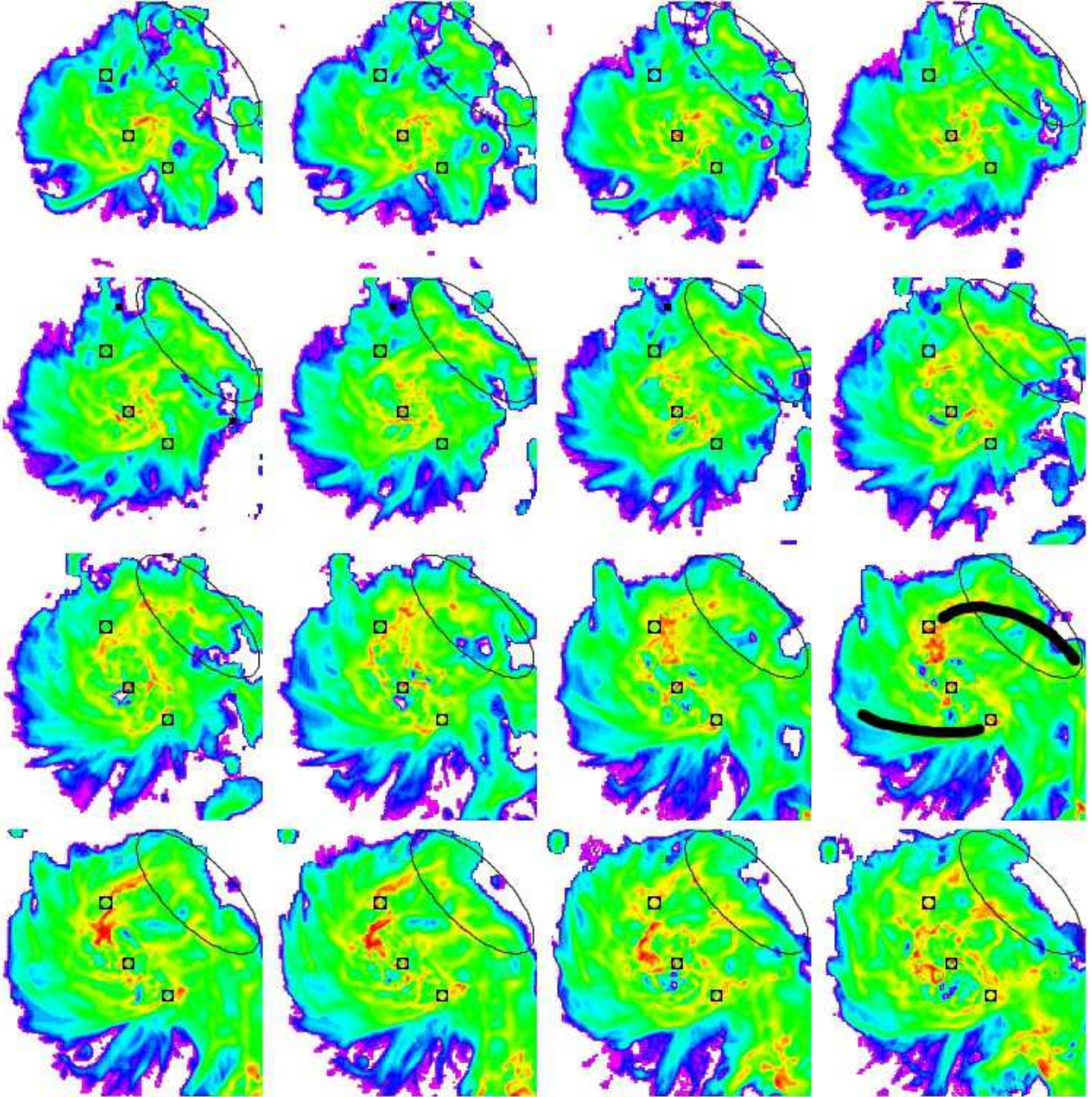


Figure 5. Evolution of the gas surface density of V27, in time intervals of 10 Myr. Time increases from top-left to bottom-right. The rightmost panel of the third row (marked with the direction of the streams) coincides with the top-left panel of Figure 4. The three black squares are located at the same positions as in Figure 4. Dense, low-metallicity stream gas is coming from the right side of the view (marked by an ellipse) and accumulates material in the top-left side of the galaxy, increasing the gas surface density and the SFR in that region. These star-forming clumps are dispersed after ~ 50 Myr, i.e., a few times the disc dynamical time.

5 GAS INFLOW

The inflowing gaseous streams join the disk through an outer ring, that can be tilted at large radii and then gradually aligned with the galaxy disk at low radii (Danovich et al. 2015). This implies that the streams join the disk generally within a plane and at a given point in angle ϕ , which may change as the streams-plus-galaxy system evolves. Figure 4 shows an example of gas accretion through streams (V27

at $z = 3.8$). Two streams coming from the circumgalactic medium can be seen at the left and right sides of the maps. They are characterized by their low metallicities, high speed and inflow. The streams meet the galaxy around the regions marked with two off-centered squares in Figure 4. In these regions, gas accumulates and drives high SFR and high $H\alpha$ luminosities (Figure 1). The $H\alpha$ -weighted metallicity of these $H\alpha$ -bright clumps is much lower than the average metallicity in the galaxy. Therefore, these metallicity drops

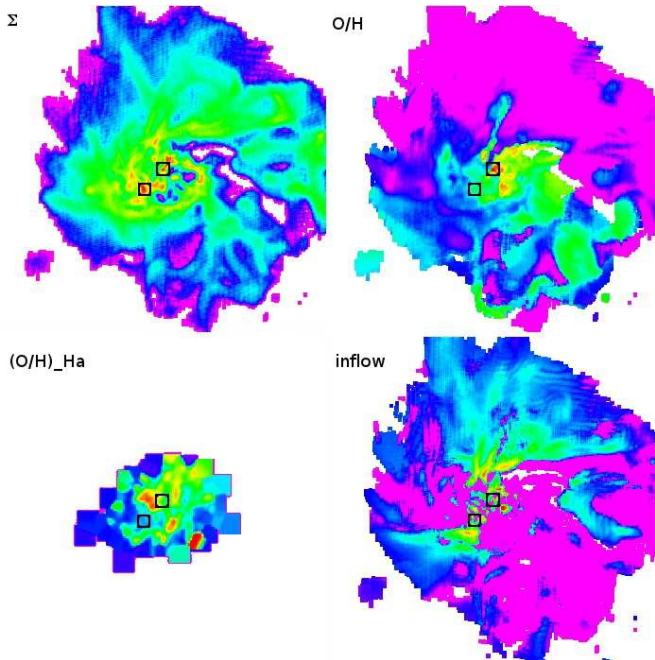


Figure 6. Face-on maps of gas surface density (Σ), mass-weighted gas metallicity (O/H), gas metallicity weighted by $H\alpha$ emissivity ($O/H_{H\alpha}$), and radial inflow of V02 at $z = 2.7$. In each panel, two square apertures mark the galaxy center and the off-centered clump. The size of the images is 20×20 kpc². The color palette is the same as in Figure 4.

mark regions where low-metallicity streams accumulate material in the galaxy.

Figure 5 shows the temporal evolution of the gas in time steps of 10 Myr, 110 Myr before the snapshot shown in Figure 4. In this sequence, relatively dense low-metallicity gas is coming from the right side of the view. This stream of inflowing gas accumulates material in the top-left side of the galaxy, increasing the gas surface density and the SFR in that region. Therefore, gas accretion into galaxies promotes an $H\alpha$ -bright burst of low-metallicity. After ~ 50 Myr, a few times the disc dynamical time, these star-forming clumps dissolve due to the combination of radiative feedback (Moody et al. 2014) and turbulent motions (Yang & Krumholz 2012). The low metallicity drops are signatures or hints of recent gas accretion into galaxies.

Figure 6 shows another example of the link between metallicity drops and gas inflow. In V02, the off-centered clump is much closer to the galaxy centre than in the previous case. As shown in Figure 4, low-metallicity gas wraps around the galaxy. The metal-poor clump, according to its $H\alpha$ -weighted metallicity, is located at the end of one of the inflowing streams (at the bottom of the clump). Other cases show similar patterns of gas accretion.

We can quantify this gas accretion by following the evolution of the gas mass within a sphere of fixed radius, $0.15R_{\text{vir}}$. Figure 7 shows this temporal evolution for gas and stars of the clumpy and non-clumpy galaxies shown in Figure 1 and Figure 2. Masses are normalized to the value at the selected snapshot (Table 1). We choose a time interval of ± 0.1 Gyr around the snapshot, so we can quantify the inflow (or outflow) before (and after) that moment captured

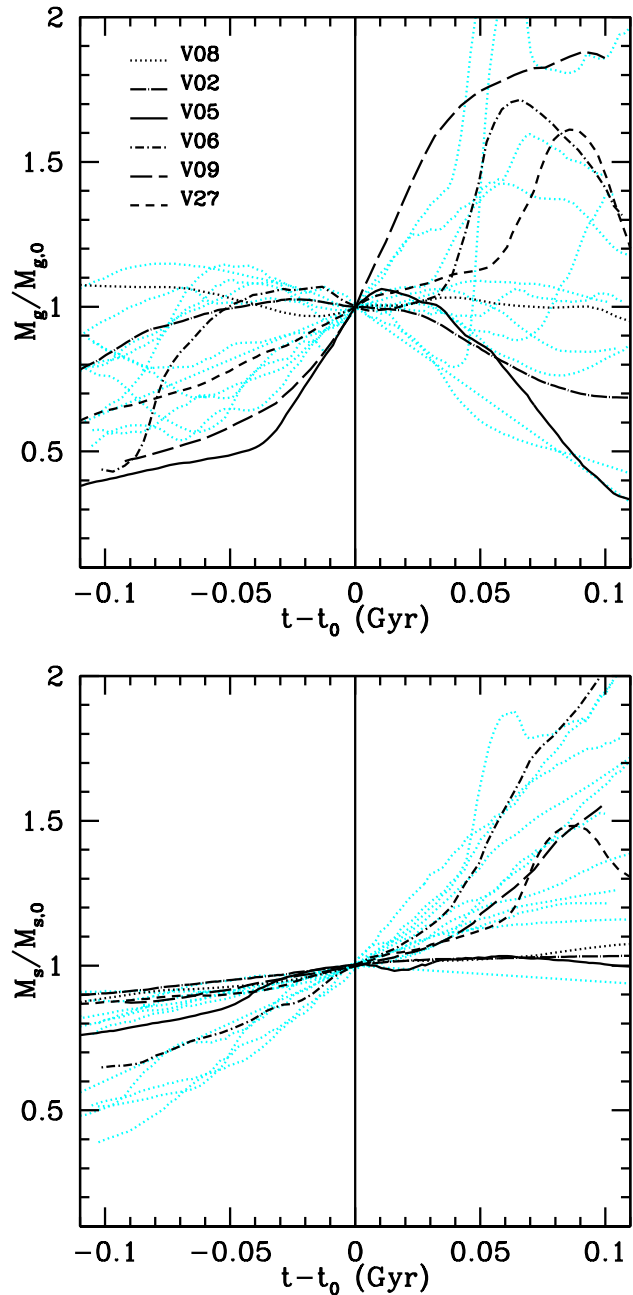


Figure 7. Evolution of the gas mass (top) and stellar mass (bottom) within $0.15R_{\text{vir}}$ of the galaxies shown in Figure 1 and Figure 2. In all the five clumpy galaxies with metallicity drops induced by gas accretion (labeled), there is a significant increase in the amount of gas within ~ 0.1 Gyr before the selected snapshots at t_0 . Cyan dotted lines correspond to the non-clumpy galaxies. There is no significant stellar accretion with the exception of the mergers between 0.05 and 0.09 Gyr after t_0 .

in Figure 1 and we allow some time for the formation of clumps from this inflow material.

In three out of five cases with metallicity drops, there is a steep increase in the gas mass in a period of 0.1 Gyr before the selected snapshot. The gas mass doubles within this period. The increase in gas is not related with merger events, because there is no sudden increase of the stellar mass within the same period. Instead, the stellar mass increases slowly,

about 10-20%, due to star-formation within the selected sphere. A exception is a merger event in V27 at 0.08 Gyr. Therefore, the increase of gas mass in these galaxies with metallicity drops is due to the continuous infall of gas from cosmic streams.

6 SUMMARY AND DISCUSSION

We addressed the continuous gas accretion of low metallicity gas into star-forming galaxies at different redshifts, using a set of zoom-in AMR cosmological simulations of galaxy formation. In $\sim 50\%$ of the cases at redshifts lower than 4, the accretion gives rise to star-forming, $H\alpha$ -bright, off-centre clumps. Most of these clumps have gas metallicities, weighted by $H\alpha$ luminosity, lower than the average metallicity in the surrounding interstellar medium. The typical values of these metallicity drops are around 0.3-0.5 dex, consistent with observations (Cresci et al. 2010; Sánchez Almeida et al. 2013, 2014b, 2015). Therefore, the observed metallicity drops can be considered as evidence for rapid gas accretion coming from cosmological inflow of low-metallicity gas.

Low metallicity inhomogeneities are dispersed in ~ 50 Myr, only a few times the disc dynamical time, $t_d = r_d/v_d = 2 \text{ kpc}/100 \text{ km s}^{-1} = 20$ Myr, where r_d and v_d are the characteristic radius and rotational velocity of these galaxies. Therefore, low-metallicity gas gets mixed with galactic interstellar medium in less than an orbital period. These short time-scales are consistent with the time-scales for dispersion of non-axisymmetric inhomogeneities in galaxy discs (Petit et al. 2015). The metal mixing is led by shear and turbulence, driven by gravitational disc instabilities. Shear accelerates the diffusion of metals by transferring inhomogeneities from large scales to small scales, where turbulence is able to dissipate them in a dynamical time-scale (Yang & Krumholz 2012). Feedback may also contribute to the dispersion of metals by the disruption of the small metal-poor clumps (Moody et al. 2014). More massive galaxies hosting giant, long-lived clumps (Dekel et al. 2009; Ceverino et al. 2010; Mandelker et al. 2014; Bournaud et al. 2014), may have metallicity drops with longer lifetimes, if clump self-enrichment due to supernovae yields is not a relevant process. Future work focused on these giant clumps will clarify these issues.

ACKNOWLEDGMENTS

The simulations were performed at the National Energy Research Scientific Computing Center (NERSC) at Lawrence Berkeley National Laboratory, and at NASA Advanced Supercomputing (NAS) at NASA Ames Research Center. This work has been partly funded by the Spanish Ministry of Economy and Competitiveness, projects AYA2012-32295 and AYA2013-47742-C04-02-P.

REFERENCES

Bournaud F., Perret V., Renaud F., Dekel A., Elmegreen B. G., Elmegreen D. M., Teyssier R., Amram P., Daddi E.,

- Duc P.-A., Elbaz D., Epinat B., Gabor J. M., Juneau S., Kraljic K., Le Floch' E., 2014, *ApJ*, 780, 57
 Bryan G. L., Norman M. L., 1998, *ApJ*, 495, 80
 Ceverino D., Dekel A., Bournaud F., 2010, *MNRAS*, 404, 2151
 Ceverino D., Dekel A., Mandelker N., Bournaud F., Burkert A., Genzel R., Primack J., 2012, *MNRAS*, 420, 3490
 Ceverino D., Klypin A., 2009, *ApJ*, 695, 292
 Ceverino D., Klypin A., Klimek E. S., Trujillo-Gomez S., Churchill C. W., Primack J., Dekel A., 2014, *MNRAS*, 442, 1545
 Chabrier G., 2003, *PASP*, 115, 763
 Cresci G., Mannucci F., Maiolino R., Marconi A., Gnerucci A., Magrini L., 2010, *Nature*, 467, 811
 Danovich M., Dekel A., Hahn O., Ceverino D., Primack J., 2015, *MNRAS*, 449, 2087
 de Avillez M. A., Mac Low M.-M., 2002, *ApJ*, 581, 1047
 Dekel A., Sari R., Ceverino D., 2009, *ApJ*, 703, 785
 Dekel A., Zolotov A., Tweed D., Cacciato M., Ceverino D., Primack J. R., 2013, *MNRAS*, 435, 999
 Edmunds M. G., Greenhow R. M., 1995, *MNRAS*, 272, 241
 Elmegreen B. G., Elmegreen D. M., 2010, *ApJ*, 722, 1895
 Elmegreen D. M., Elmegreen B. G., Ravindranath S., Coe D. A., 2007, *ApJ*, 658, 763
 Elmegreen D. M., Elmegreen B. G., Sánchez Almeida J., Muñoz-Tuñón C., Putko J., Dewberry J., 2012, *ApJ*, 750, 95
 Fisher D. B., Bolatto A. D., Herrera-Camus R., Draine B. T., Donaldson J., Walter F., Sandstrom K. M., Leroy A. K., Cannon J., Gordon K., 2014, *Nature*, 505, 186
 Genzel R., Newman S., Jones T., Förster Schreiber N. M., Shapiro K., et al. 2011, *ApJ*, 733, 101
 Guo Y., Ferguson H. C., Bell E. F., Koo D. C., Conselice C. J., et al. 2015, *ApJ*, 800, 39
 Kehrig C., Vílchez J. M., Pérez-Montero E., Iglesias-Páramo J., Brinchmann J., Kunth D., Durret F., Bayo F. M., 2015, *ApJ*, 801, L28
 Kennicutt Jr. R. C., 1998, *ApJ*, 498, 541
 Kennicutt Jr. R. C., Calzetti D., Walter F., Helou G., Hollenbach D. J., et al. 2007, *ApJ*, 671, 333
 Kravtsov A. V., 2003, *ApJ*, 590, L1
 Kravtsov A. V., Klypin A. A., Khokhlov A. M., 1997, *ApJS*, 111, 73
 Magrini L., Corbelli E., Galli D., 2007, *A&A*, 470, 843
 Mandelker N., Dekel A., Ceverino D., Tweed D., Moody C. E., Primack J., 2014, *MNRAS*, 443, 3675
 Moody C. E., Guo Y., Mandelker N., Ceverino D., Mozena M., Koo D. C., Dekel A., Primack J., 2014, *MNRAS*, 444, 1389
 Petit A. C., Krumholz M. R., Goldbaum N. J., Forbes J. C., 2015, *MNRAS*, 449, 2588
 Pilyugin L. S., Grebel E. K., Zinchenko I. A., 2015, *MNRAS*, 450, 3254
 Queyrel J., Contini T., Kissler-Patig M., Epinat B., Amram P., Garilli B., Le Fèvre O., Moultaqa J., Paioro L., Tasca L., Tresse L., Vergani D., López-Sanjuan C., Pérez-Montero E., 2012, *A&A*, 539, A93
 Richards S. N., Schaefer A. L., López-Sánchez Á. R., Croom S. M., Bryant J. J., et al. 2014, *MNRAS*, 445, 1104
 Sánchez S. F., Rosales-Ortega F. F., Iglesias-Páramo J., Mollá M., Barrera-Ballesteros et al. 2014, *A&A*, 563, A49

- Sánchez Almeida J., Muñoz-Tuñón C., Elmegreen D. M., Elmegreen B. G., Méndez-Abreu J., 2013, *ApJ*, 767, 74
- Sánchez Almeida J., Elmegreen B. G., Muñoz-Tuñón C., Elmegreen D. M., 2014a, *A&A Rev.*, 22, 71
- Sánchez Almeida J., Morales-Luis A. B., Muñoz-Tuñón C., Elmegreen D. M., Elmegreen B. G., Méndez-Abreu J., 2014b, *ApJ*, 783, 45
- Sánchez Almeida J., Elmegreen B. G., Muñoz-Tuñón C., Elmegreen D. M., Pérez-Montero E., Amorín R., Filho M. E., Ascasibar Y., Papaderos P., Vílchez J. M., 2015, *ApJ*, 810, L15
- Stott J. P., Sobral D., Swinbank A. M., Smail I., Bower R., Best P. N., Sharples R. M., Geach J. E., Matthee J., 2014, *MNRAS*, 443, 2695
- Tadaki K.-i., Kodama T., Tanaka I., Hayashi M., Koyama Y., Shimakawa R., 2014, *ApJ*, 780, 77
- van de Voort F., Schaye J., 2012, *MNRAS*, 423, 2991
- van Zee L., Salzer J. J., Haynes M. P., O'Donoghue A. A., Balonek T. J., 1998, *AJ*, 116, 2805
- Verbeke R., De Rijcke S., Koleva M., Cloet-Osselaer A., Vandenbroucke B., Schroyen J., 2014, *MNRAS*, 442, 1830
- Woolsey S. E., Weaver T. A., 1995, *ApJS*, 101, 181
- Yang C.-C., Krumholz M., 2012, *ApJ*, 758, 48
- Zolotov A., Dekel A., Mandelker N., Tweed D., Inoue S., DeGraf C., Ceverino D., Primack J. R., Barro G., Faber S. M., 2015, *MNRAS*, 450, 2327

This paper has been typeset from a $\text{\TeX}/\text{\LaTeX}$ file prepared by the author.